


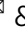



Machine learning-derived reaction statistics for 3D spectroimaging of copper sulfidation in heterogeneous rubber/brass composites

Hirosuke Matsui^{1,2,3} , Yuta Muramoto^{1,2,3}, Ryusei Niwa^{1,2,3}, Takashi Kakubo⁴, Naoya Amino⁴, Tomoya Uruga⁵, Minh-Quyet Ha⁶ , Duy-Tai Dinh⁶ , Hieu-Chi Dam⁶  & Mizuki Tada^{1,2,3,7,8} 

The sulfidation of copper derived from copper-zinc alloy (brass) in sulfur-containing rubber, used for plating steel-cord-reinforced rubber tires, is suggested to be the key reaction for the adhesive behavior between brass and rubber in tires. However, the heterogeneous structures of rubber/brass interfaces have prevented us from understanding the sulfidation of metallic copper in brass and the formation of copper sulfides at the brass surface and buried rubber interface. Here, we visualize the 3D spatial location and chemical states of copper species in a rubber/brass composite during its aging process by 3D X-ray spectroimaging with X-ray absorption fine structure-computed tomography. Machine learning-derived reaction statistics of the 3D spectroimaging data reveal the reaction mechanism of copper sulfidation in the heterogeneous rubber/brass composite.

¹Department of Chemistry, Graduate School of Science, Nagoya University, Furo, Chikusa, Nagoya, Aichi 464-8602, Japan. ²Integrated Research Consortium on Chemical Science, Nagoya University, Furo, Chikusa, Nagoya, Aichi 464-8602, Japan. ³RIKEN SPring-8 Center, Koto, Sayo, Hyogo 679-5198, Japan. ⁴Materials Performance Laboratory, Research and Advanced Development Division, The Yokohama Rubber Co., Ltd., Oiwake, Hiratsuka, Kanagawa 254-8601, Japan. ⁵Japan Synchrotron Radiation Center, SPring-8, Koto, Sayo, Hyogo 679-5198, Japan. ⁶School of Knowledge Science, Japan Advanced Institute of Science and Technology, Asahidai, Nomi, Ishikawa 923-1291, Japan. ⁷Research Center for Materials Science, Nagoya University, Furo, Chikusa, Nagoya, Aichi 464-8602, Japan. ⁸Institute for Advanced Study, Nagoya University, Furo, Chikusa, Nagoya, Aichi 464-8602, Japan. ✉email: dam@jaist.ac.jp; tada.mizuki.u6@f.mail.nagoya-u.ac.jp

Steel-cord-reinforced rubber tires are widely used in automobiles and steel cords are commonly plated with Cu-Zn alloy (brass) as corrosion-resistant coating¹. Strong adhesion between rubber and brass-plated steel cord is crucial for the long-term use of belted radial tires and the actual structure of the adhesive interface between rubber and brass-plated steel cord has been extensively investigated². Cu and Zn sulfides are formed at the rubber/steel cord interface through the passive state of ZnO on brass-plated steel cord and these interlayers are thought to be related to the adhesion behaviors of the rubber/brass composite^{3–7}.

In particular, the sulfidation of Cu at the buried interface in rubber is suggested to be vital for the strong adhesion of rubber and brass composite, and the formation of non-stoichiometric Cu sulfide (close to Cu₂S) increases the adhesion strength of rubber and brass^{8–11}. Spectroscopic analyses of adhesion interfaces have been investigated by X-ray diffraction^{12–14}, X-ray photoelectron spectroscopy (XPS)^{11,15–20}, and hard X-ray photoelectron spectroscopy (HAXPES)^{5,21}, and changes in chemical composition at the adhesion interface were identified as the key factors in the deterioration of adhesion between rubber and brass. However, the spatial and chemical heterogeneities of rubber composite samples present a major challenge in understanding interfacial adhesion and the sulfidation and desulfurization reactions of Cu species at the buried rubber/brass interface are still unclear in the three-dimensional (3D) structures of the heterogeneous rubber/brass composite materials.

The interfacial adhesive layers with the Cu sulfides are gradually degraded as rubber tires are used. 3D focused-ion-beam SEM-EDS and STEM-EDS images have shown the formation of large voids and localized Cu_xS ($x = 1.8–2$) clumps at the buried interface of the rubber and steel cord after thermal aging treatments with moisture^{22–26}. Heating with moisture caused further oxidation and sulfidation of the adhesive Cu sulfide layers in the tire composite, deteriorating the non-stoichiometric Cu sulfide layer and reducing the adhesive property. Although the rubber/brass adhesion has been evaluated by mechanical stress tests^{27,28}, there is no spatial information about the Cu sulfidation reactions and changes in the buried adhesion interface structure in the heterogeneous 3D rubber/brass composite.

Hard X-ray/neutron scattering techniques^{29,30} and CT^{31–34} of rubber-filler composites were used in the pioneering analysis of rubber materials, but the spectroimaging of the sulfidation of brass Cu species in rubber composites has not yet been reported. Hard X-ray spectroimaging, which is the most powerful tool for visualizing chemical information in bulk materials non-destructively^{35–38}, and Hard X-ray absorption fine structure spectroscopy with computed tomography (XAFS-CT) is performed by CT with different X-ray energies and provides 3D images of spectroscopic information, such as amount, valence state, and local coordination of each chemical species in composite materials^{39–42}. In this paper, we report the 3D X-ray spectroimaging of the adhesion layers of a rubber/brass composite, which showed the Cu sulfidation reactions in the rubber/brass composite during tire aging. Data-driven machine learning using the 3D spectroimaging data tracked step by step for the aging processes successfully revealed the stepwise transition of Cu sulfidation and desulfurization in the rubber/brass composite.

Results and discussions

3D visualization of the rubber/brass composite for the aging step by XAFS-CT imaging. A rubber sample mixed with around 2000 brass clumps (Cu/Zn ratio = 75/25, $\phi 3 \mu\text{m} \times 0.2 \mu\text{m}$; 1 wt % with respect to rubber) was prepared and the rubber/brass composite was heated at 443 K for 10 min to prepare adhesive

layers between the rubber and the brass clumps (Supplementary Methods 1, Supplementary Figs. 1–3, Supplementary Table 1, and Supplementary Note 1). Cu *K*-edge XAFS-CT spectroimaging of the vulcanized rubber composite fixed in a polyimide capillary tube was performed at the SPring-8 synchrotron facility (Supplementary Methods 2 and Supplementary Fig. 3)⁴³. After the first XAFS-CT spectroimaging measurement of the as-vulcanized sample, the rubber/brass composite was treated at 343 K under the relative humidity of 96% for 3 days for the first aging treatment and then the second XAFS-CT spectroimaging was conducted again on the same composite. The cycle of the aging treatment followed by the XAFS-CT spectroimaging was repeated three times and the series of XAFS-CT data was collected for the same rubber/brass composite sample after the aging times of 0, 3, 14, and 28 days (samples **Aging-0**, **Aging-3**, **Aging-14**, and **Aging-28**, respectively) (Supplementary Fig. 1). The evaluation of adhesion behavior between brass and rubber has been performed by the ASTM D2229-02 standard test, which is one of the typical pullout tests developed and published by the ASTM International (the American Society for Testing and Materials). A similar pullout test for brass-plated tire samples (195/65R15 size) was conducted for similar aging processes. The original adhesion force before aging (just after vulcanization of the rubber sample) was 176 N inch⁻¹, and it was decreased to 149 N inch⁻¹ after the 14-days aging and 138 N inch⁻¹ after the 28-days aging, suggesting the present aging conditions significantly decrease the adhesive strength of the brass/rubber interface.

Cu *K*-edge XAFS-CT spectroimaging was conducted by the repetition of X-ray energy quick-scans around the Cu *K*-edge ($E = 8857–9357 \text{ eV}$) recording two-dimensional (2D) X-ray transmission images at different projection angles (θ). Changing the projection angles θ from -90° to 90° provided the series of XAFS-CT transmission images (Supplementary Fig. 4). The series of the 2D transmission images in the Cu *K*-edge X-ray absorption near-edge structure (XANES) region was converted to the X-ray absorption coefficient (μt) (Supplementary Methods 3 and Supplementary Fig. 5), and each spatially resolved XANES spectrum in $1.3 \mu\text{m} \times 1.3 \mu\text{m}$ area on the 2D μt image was fitted with the linear combination of the XANES spectra of three standard Cu components, namely, metallic Cu in brass (denoted as Cu (brass)), monovalent Cu₂S, and bivalent CuS (Supplementary Fig. 6). The extracted structural parameters for morphology, Cu density, and the local amounts of the three Cu species in the 2D images at each θ were finally reconstructed into 3D images in real space.

The rubber/brass composite contained Zn in brass, ZnO passive film on the brass surface, and ZnO loaded in the rubber as a vulcanization activator (Supplementary Note 1, Supplementary Table 1, and Supplementary Fig. 2). Several reactions involving ZnO have been reported as Cu reactions on the ZnO passive film of brass surface, which affect the adhesion between rubber and brass¹⁵ and the formation of Zn stearate in the rubber⁴⁴. However, XAFS/XAFS-CT spectra at the Zn *K*-edge overlapped with those at the Cu *K*-edge and it was not suitable to analyze Zn species from brass (Zn amount with one of the third of the Cu amount in the brass) by the similar imaging analysis. Co stearate, which was added to the rubber sample as a vulcanization activator (Supplementary Note 1, Supplementary Table 1, and Supplementary Fig. 2), was not detected by hard X-ray XAFS-CT at the Co *K*-edge because of its low Co loading (2 phr in the rubber sample).

The Cu *K*-edge XANES spectra of the rubber/brass composite sample for the aging processes measured in the same view as XAFS-CT imaging are presented in Supplementary Fig. 7b, suggesting the changes in the local structures of the Cu species in the sample by aging. Decreases in the intensity of the pre-edge

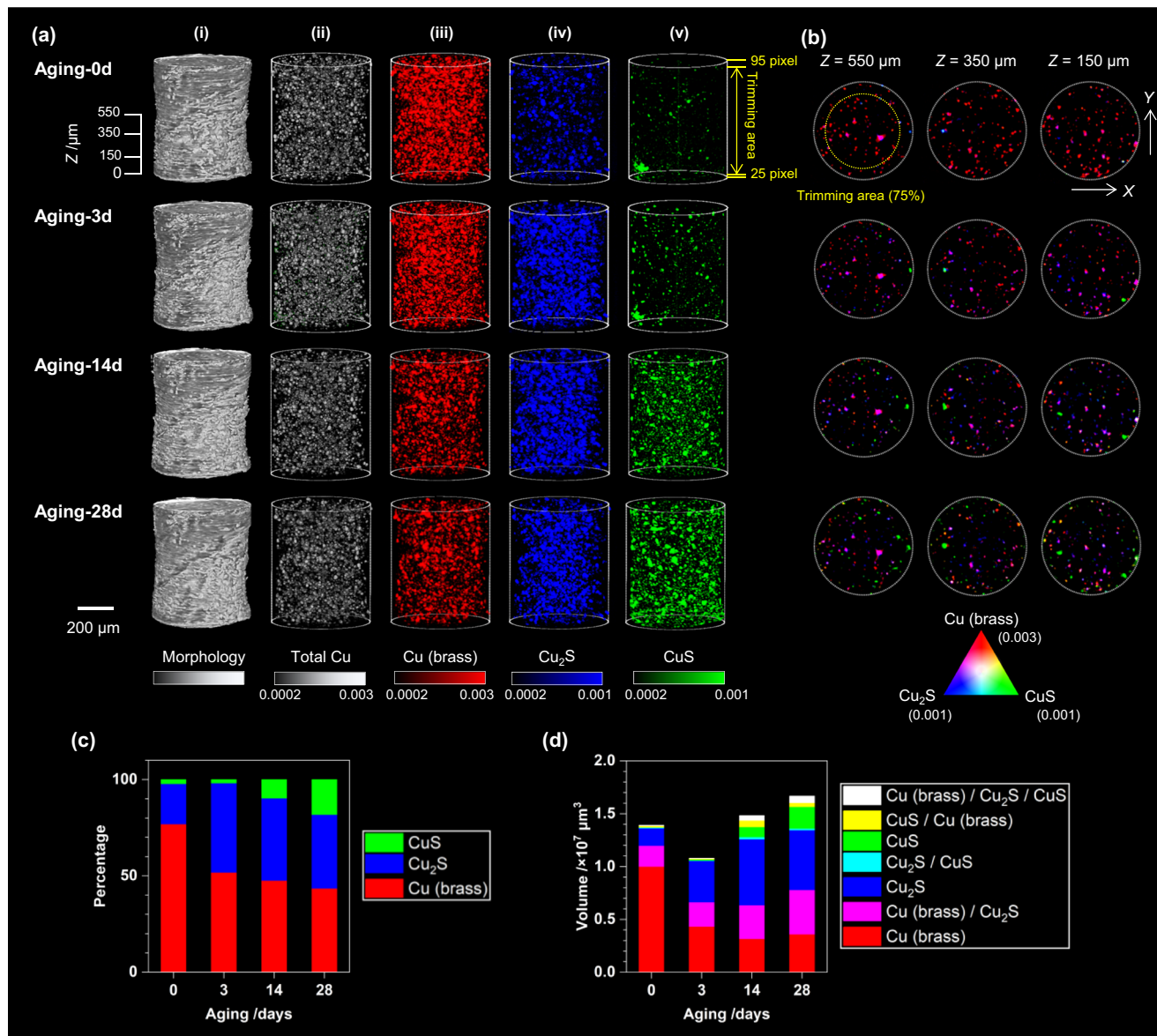


Fig. 1 The 3D spatial location and chemical states of copper species in a rubber/brass composite during aging. **a** Reconstructed 3D images of (i) morphology, (ii) Cu distribution relative to total Cu atom, (iii) metallic Cu (brass) distribution, (iv) monovalent Cu₂S distribution, and (v) bivalent CuS distribution in the rubber/brass composite visualized by Cu K-edge XAFS-CT. **b** Representative cross-sectional images of the 3D images at Z of 550, 350, and 150 μm heights. The description of color contrast is presented in Supplementary Fig. 9. Yellow lines (75% of the sample diameter and the positions of the top 95 layers and the bottom 25 layers along Z) indicate the trimming area for further informatics analysis. **c** Ratios of the absolute amounts of the three Cu species in the rubber/brass composite. **d** Calculated volumes base on the voxels where the Cu species were detected.

peak at 8975.0 eV, increases in the intensity at 8991.4 eV, and increases in the intensity at 9018.4 eV were clearly found against the aging time, reflecting the trends of Cu sulfurization by the aging process. The reconstructed 3D images (Z = 0–1180 μm) of the sample morphology, the total Cu amount, and the local distributions of Cu (brass), Cu₂S, and CuS in the rubber/brass composite are presented in Fig. 1a. The 3D image (Fig. 1a–i) showed the 3D morphology of the rubber/brass composite sample, and the similarity in the morphology images of the sample for the four different aging times suggested that the XAFS-CT spectroimaging successfully provided the same field of view of the rubber/brass. The absolute amounts of the three Cu components were estimated by the summation of the observed intensities of the three Cu species (Fig. 1c) and their spatial volumes were estimated from the volumes of the component voxels where any Cu species were detected in the 3D image

(Fig. 1d). The ratios of the amounts of Cu (brass), Cu₂S, and CuS were calculated from the sum of the intensities of each Cu species for all voxels in the field of view, and they were 0.77/0.21/0.02 (Aging-0d), 0.52/0.46/0.02 (Aging-3d), 0.47/0.43/0.10 (Aging-14d), and 0.44/0.38/0.18 (Aging-28d), respectively (Fig. 1c). Cu (brass) was the major species in the fresh sample (Aging-0d) and the first aging treatment significantly produced Cu₂S via the consumption of the metallic Cu (brass) (Aging-3d). Further aging treatments gradually decreased the amount of Cu (brass) and produced CuS without increases in the ratio of Cu₂S in the rubber composite.

The volumes of the voxels of the three Cu components were detected and the quantitated volumes of the single or mixture of the three Cu components were presented in Fig. 1d. The ratios of the spatial volumes were slightly different from those of the absolute amounts of the three Cu species, reflecting differences in the

dispersion and densities of the three Cu species in the rubber sample. In the rubber composite before aging (**Aging-0d**), most of the voxels in which Cu was detected were assigned as Cu (brass), which agreed with Fig. 1c. The voxels in which Cu₂S was detected contained Cu₂S only (blue) or a mixture of Cu (brass) and Cu₂S (pink), and the latter accounted for 54% of these voxels where Cu₂S was detected, indicating that Cu₂S tends to be formed close to the brass clumps within the voxel size (1.3 μm × 1.3 μm × 1.3 μm). In **Aging-3d**, the volume of overall Cu voxels in the rubber sample was substantially decreased (78% of that of **Aging-0d**, Fig. 1d). As the Cu (brass) species were consumed, the volume of Cu₂S (blue) increased. The number of voxels of the mixture of Cu (brass) and Cu₂S (pink) was smaller than that of Cu₂S (blue), indicating that the diffusion of Cu₂S proceeded from the brass surface into the rubber matrix. The similarity in the volumes of Cu (brass) (red) voxels in **Aging-14d** suggested that further aging treatment does not cause much sulfidation of brass, but an increase in the volume of Cu₂S was clearly observed in **Aging-14d**. The total volume of Cu in the rubber sample was also increased, indicating the diffusion of the copper sulfide species in the rubber matrix. The small volume of CuS (green) compared with that of Cu₂S (blue) suggested that the formed CuS species was localized in the rubber matrix. In **Aging-28d**, similar trends were observed, and the consumption of Cu₂S and the formation of CuS were greater, indicating that several reactions occurred in the rubber matrix with changing the amounts and volumes of the Cu components.

Infography for the reaction of Cu species in the rubber by data-driven machine learning. The statistical amount of the brass clumps (around 2000 clumps) in the rubber composite sample allowed us to perform machine-learning data-driven analysis to understand the Cu sulfidation mechanism for the aging processes. It was expected that tracking the variation of the structures and chemical states of the 2000 brass clumps in the aging process accompanied by the Cu sulfidation reaction could identify the reaction mechanism of the formation and consumption of adhesive Cu layers at the brass/rubber interface^{45–47}. However, the fluctuation of the positions, shapes, structures, and chemical states of the brass clumps in the rubber composite during the aging treatments required the matching of observed Cu clumps in the images over the four aging times (**Aging-0d**, **Aging-3d**, **Aging-14d**, and **Aging-28d**). Thus, we investigated a data-driven informatics approach to match the brass clumps with changes in the positions, shapes, structures, and chemical states and allow the Cu sulfidation reactions of each brass clump identified in the 3D images to be tracked for each aging treatment.

The method of tracking Cu clumps and reactions in the rubber composite consisted of the following steps: detecting and matching all Cu clumps at different aging times, fitting the distribution of the intensity at voxels belonging to each Cu valence state in the clumps to a log-normal distribution for each valence state, describing each clump using the fitted parameters as descriptors, and applying an unsupervised learning method to identify the patterns of interchange between the three Cu valence states in the Cu clumps. The coordinate axes of the voxels in the sample at the four aging times were transformed and unified for tracking the changes in the Cu species during the aging treatments. Among approximately 2000 of Cu clumps identified in the 3D images visualized, matched sequences for all four aging times were tracked for 802 of Cu clumps, which were used for further unsupervised machine learning.

Figure 2 shows the 3D images of two typical brass clumps in the rubber/brass composite, for which the alignment during the four aging times was tracked. Clump A located at (X, Y, Z) of (0.53, 0.42, 0.62) in Fig. 1a was 10 μm in size and had a metallic

Cu (brass) core and low-density Cu₂S overlayers before aging (Fig. 2a–i). The exterior of the original Cu (brass) in **Aging-0d** (before aging) was defined as the outer surface of the original brass clump before the Cu sulfidation and we calculated the geometric distance (d_{surf}) to the outer surface in the clumps for the four aging times. The positive values of d_{surf} indicated Euclidean distances from the original brass contours away from the clumps, and negative d_{surf} values indicated distances toward the inside of the original brass clumps. Thus, the distributions of the three Cu species as a function of d_{surf} showed the reactions of the Cu species at the brass surface and the diffusion of Cu sulfide species at the buried rubber/brass interface (Fig. 2b).

Clump B located (X, Y, Z) of (0.32, 0.38, 0.52) in Fig. 1a, which was 18 μm in size, initially had a similar state to that of clump A, and red Cu (brass) surface was clearly observed as shown in Fig. 2a–v. However, its sulfidation was found to be widely different from that of clump A. The consumption of Cu (brass) was moderate and most of the brass clump was still present in **Aging-28d** (Fig. 2a–viii). The first 3-day aging step produced Cu₂S and the further aging steps also produced CuS (Fig. 2b–vi–viii). The formation of CuS was observed both inside the space of the original brass clump and outside of the original crump surface, indicating that the CuS formation proceeded between the gap of the brass particles composed of the original brass clump B and it diffused to the rubber side by aging.

The different reaction behaviors of the brass clumps indicate the variety of the Cu sulfidation in the rubber/brass composite during aging. We applied a data-driven informatics approach to the matched 802 brass clumps to track the series of sulfidation reactions over the four aging times and performed a statistical analysis of the sulfidation for the 802 brass clumps in the rubber composite. Each clump of the matched 802 brass clumps had three sets of amount data for metallic Cu (brass), monovalent Cu₂S, and bivalent CuS (Supplementary Fig. 10e–h), and thus there were 9624 sets of amount data (3 Cu species × 802 clumps × 4 aging times). Figure 3a shows plots of the interquartile ratio of the log-normal Cu distribution for the 9624 data sets of the three Cu species as a function of the mass contribution of each Cu state. The vectors of changes in the amounts of each Cu species for the aging steps are presented in Fig. 3b, which shows the sequences of the reactions of the three Cu species in the 802 clumps for the aging steps. Each vector indicated how the amount and distribution of each Cu species changed in the three steps from one aging time to the next (e.g., **Aging-0** to **Aging-3**, **Aging-3** to **Aging-14**, and **Aging-14** to **Aging-28**), and the length of the reaction vector corresponded to the magnitude of a reaction, such as the high consumption of brass and the heavy sulfidation of Cu.

The reaction vectors were characteristic for each Cu species and each aging step. At the beginning of the aging process (**Aging-0** to **Aging-3**), most of the vectors of Cu (brass) pointed upward from the bottom-right edge of the plot to the left (Fig. 3b, red), suggesting the consumption of Cu (brass) during the first aging treatment. In contrast, the vectors of monovalent Cu₂S mostly pointed upward and to the right (Fig. 3b, blue), suggesting the formation of dispersed Cu₂S layers. Most of the vectors of CuS (Fig. 3b, green) were negligible and localized around the origin of the plot, indicating that most of the clumps did not form CuS for the first aging step. These results suggested that the first aging treatment tended to cause the high consumption and wear of the brass clumps and the formation of weak Cu₂S layers without CuS.

In the next aging step (**Aging-3** to **Aging-14**), there were different trends in the reaction vectors in Fig. 3b. The vectors of Cu (brass) pointed downward and to the left toward the origin of

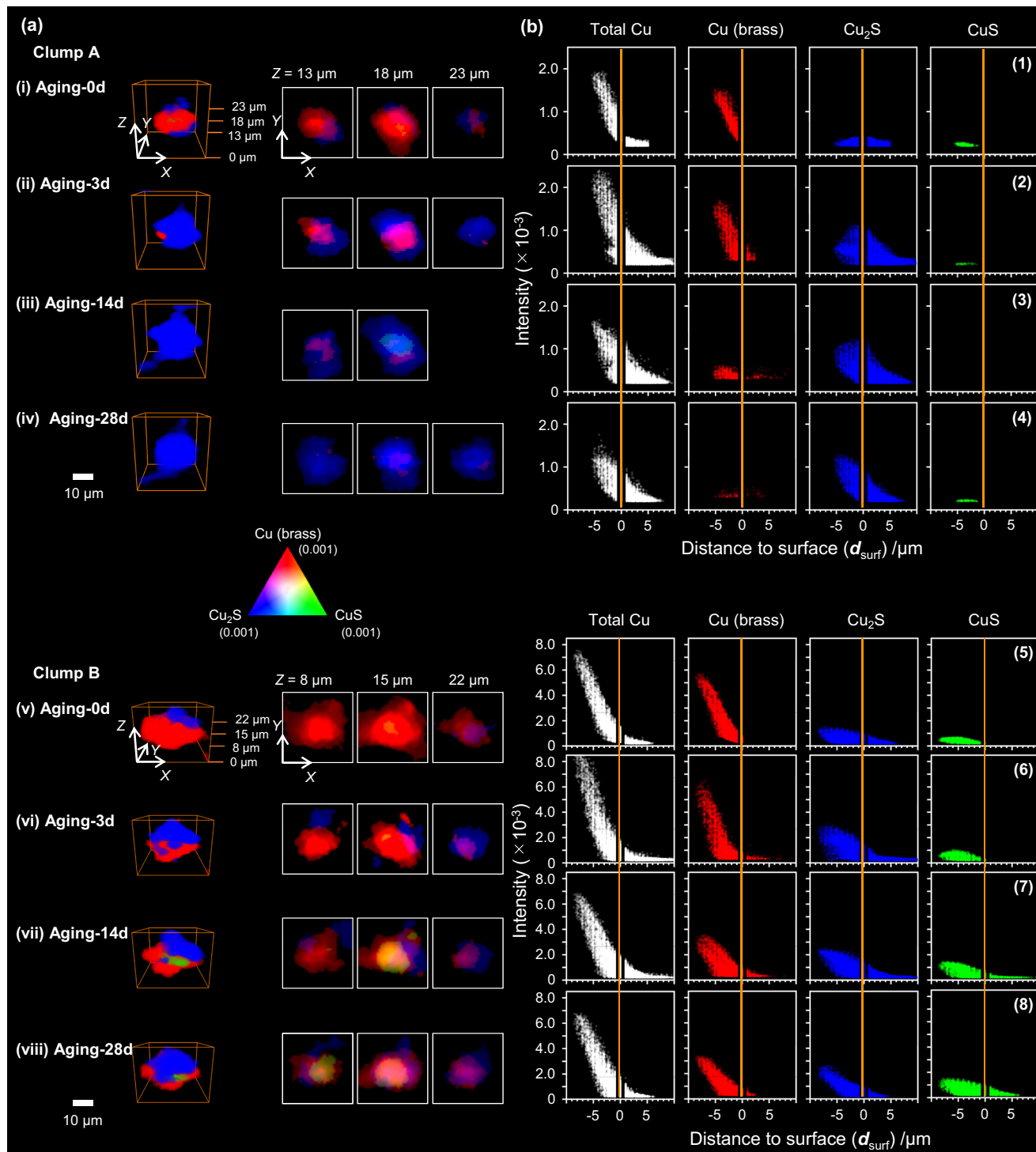


Fig. 2 Geometric analysis of representative brass clumps for degradation stages. Aging-0d (i and v), Aging-3d (ii and vi), Aging-14d (iii and vii), and Aging-28d (iv and viii) for clump A (i–iv) and B (v–viii). **a** 3D images (XYZ) with 2D cross-sections (XY) at each height (Z) and **(b)** density plots of the Cu species (total density of the three Cu species (total Cu), Cu (brass), Cu_2S , and CuS) against the calculated Euclidean distance to the original position of the brass clump surface (d_{surf}). Intensity values of <0.0002 were regarded as values within noise for the analysis.

the plot, which was widely different from those for the first aging step (upward and to the left). The left-downward trend indicated the further consumption of the worn brass clumps in this aging step. The reaction vectors of Cu_2S were more random and those of CuS became longer than those of the first aging step. These results suggested more complicated Cu sulfidation reactions in the second aging step. In the third aging step (**Aging-14** to **Aging-28**), the vector plots of all three Cu species appeared

random (Fig. 3b), but the plot of CuS showed longer shifts than those of the former steps, indicating the further progress of the CuS formation via several reaction routes in the rubber/brass composite.

The statistical number of the reaction vectors obtained by the 3D spectroimaging enabled unsupervised learning analysis with Gaussian mixture model algorithms to group the changes in the reactions of the three Cu components (ΔCu (brass), $\Delta\text{Cu}_2\text{S}$, and

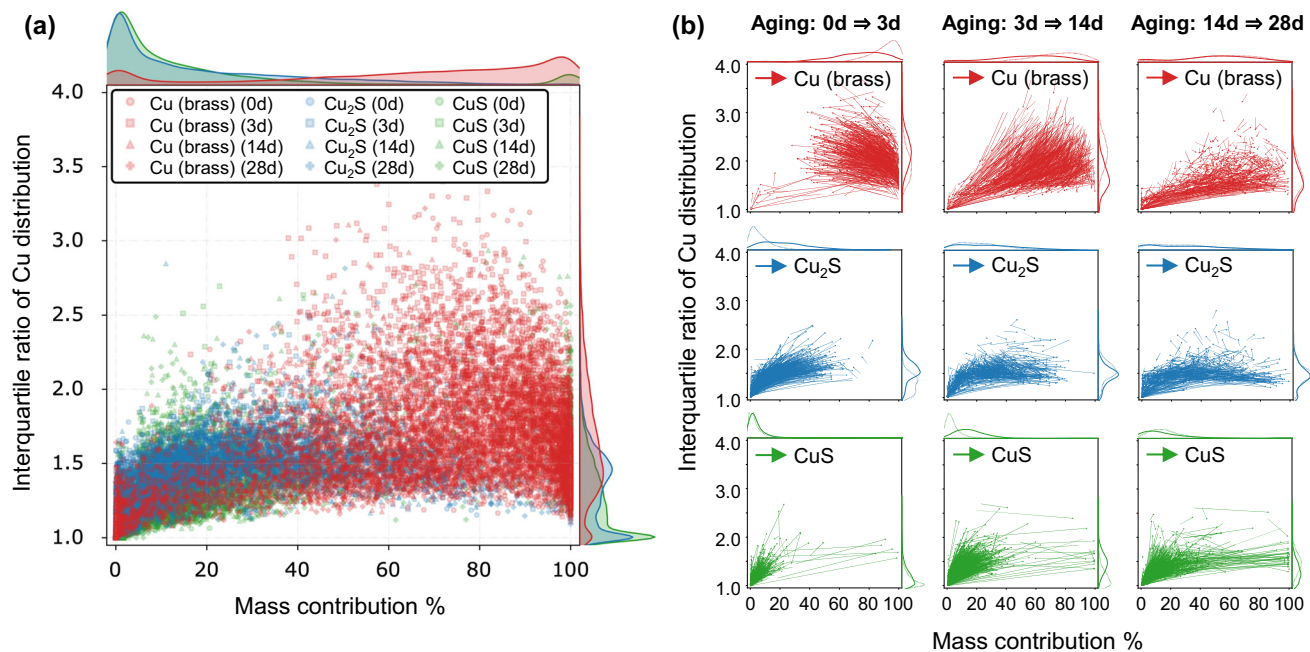


Fig. 3 Tracking of the series of Cu sulfuration reaction over the four aging times. **a** Plot of the interquartile ratio of the log-normal Cu distribution against Cu mass contribution. **b** The graphics of reaction vectors for the three Cu components at each aging stages.

Δ CuS) during the aging steps. Auto-detected groups were associated with the types of reactions, and five reaction types (types 1–5) were statistically detected by unsupervised learning, for which trends in changes between the three Cu components were significantly different as shown in Fig. 4. Types 1–3 (orange, red, and green distributions in Fig. 4a) corresponded to reactions involving the consumption of Cu (brass) (Δ Cu (brass) < 0) and the formation of Cu₂S (Δ Cu₂S > 0) in each clump, and types 1, 2, and 3 corresponded to Δ CuS of ~0, <0, and >0, respectively. Thus, reaction types 1–3 with the sulfidation and consumption of Cu (brass) to form monovalent Cu₂S corresponded to the reaction features of adhesion reinforcement in the aging treatment^{3–11,16,22}. Type 4 had different reaction features and involved the loss of Cu₂S and the formation of CuS (Δ Cu₂S < 0 and Δ CuS > 0), which were probably related to the embrittlement of the rubber/brass adhesion²². Type 5 showed the random feature of the reaction vectors, whose chemical meaning was difficult to explain.

We counted the number of clumps that were classified into the five reaction types (Fig. 4d), which clearly showed the transition of the Cu sulfidation reactions in the rubber/brass composite. From **Aging-0d** to **Aging-3d**, the major reaction type was found to be type 1, although it was a minor type subsequently (Fig. 4d). During the first aging step after the pretreatment vulcanization, the complete sulfidation of Cu to Cu₂S would proceed as the type-1 reaction with the reinforcement of adhesion behavior. From **Aging-3d** to **Aging-14d**, the reactions with the CuS formation (types 3 and 4) were found to be major, and types 1, 2, and 5 were negligible. The loss of the Cu₂S layers and the appearance of CuS in type 4 were probably caused by the embrittlement of the rubber/brass adhesion, which started in the second step of aging. The final aging step (**Aging-14d** to **Aging-28d**) caused the parallel reactions of the four reaction types (types 2–5) (Fig. 4d), indicating the complicated competition of the several Cu reaction types in the rubber/brass composite.

The chemical properties for the adhesion of rubber and brass were investigated by XPS, HAXPES, SEM, TEM, and XAFS techniques and the formation and consumption of Cu₂S have been suggested as key factors in the adhesion property^{3–11,16,22}.

The promotion of Cu₂S formation at the interface of rubber and brass and the suppression of Cu₂S consumption after the formation of the adhesive layers at the interface are essential issues for the maintenance of the adhesive behavior in rubber/brass composites^{19,22}. However, the transition of the Cu sulfidation visualized by the combination of the 3D spectroimaging and the unsupervised machine learning suggested that the desired Cu₂S formation with Cu in brass and sulfur species in rubber was saturated and almost stopped at the middle stage of aging, although it was predominant and selective in the fresh state. Instead of the further Cu₂S formation, unfavorable CuS formation via several reaction types paralleled in the aged sample was inevitable in the rubber/brass composite.

Direct imaging of chemical reactions in composite materials whose components change chemically and spatially had been difficult, but the 3D hard X-ray spectroimaging by CT imaging and XAFS spectroscopy enabled the direct visualization of the sequences of reaction characteristics with the sulfidation of Cu components in the rubber/brass composite material. An ideal composite system with statistical amounts of brass clumps and the utilization of the 3D spectroimaging and data-driven informatics allowed tracking of the transition of the Cu sulfidation features related to the rubber/brass adhesion for the first time. The present work provides a quantitative way to elucidate the manners and transitions of chemical reactions in actual heterogeneous composite materials and the further extension of the spectroimaging-driven statistical analysis using unsupervised learning to various rubber/brass composites would be promising to bring out the practical ways to improve adhesive behaviors in brass-plated steel-reinforced tires.

Conclusions

3D X-ray spectroimaging by XAFS-CT of the aging process of a heterogeneous rubber/brass composite enabled the direct visualization of Cu sulfidation and Cu diffusion in the rubber/brass composite. The big data from the 3D spectroimaging containing the geometrical feature of the heterogeneous composite, the spatial distribution of the Cu species, the chemical states of the

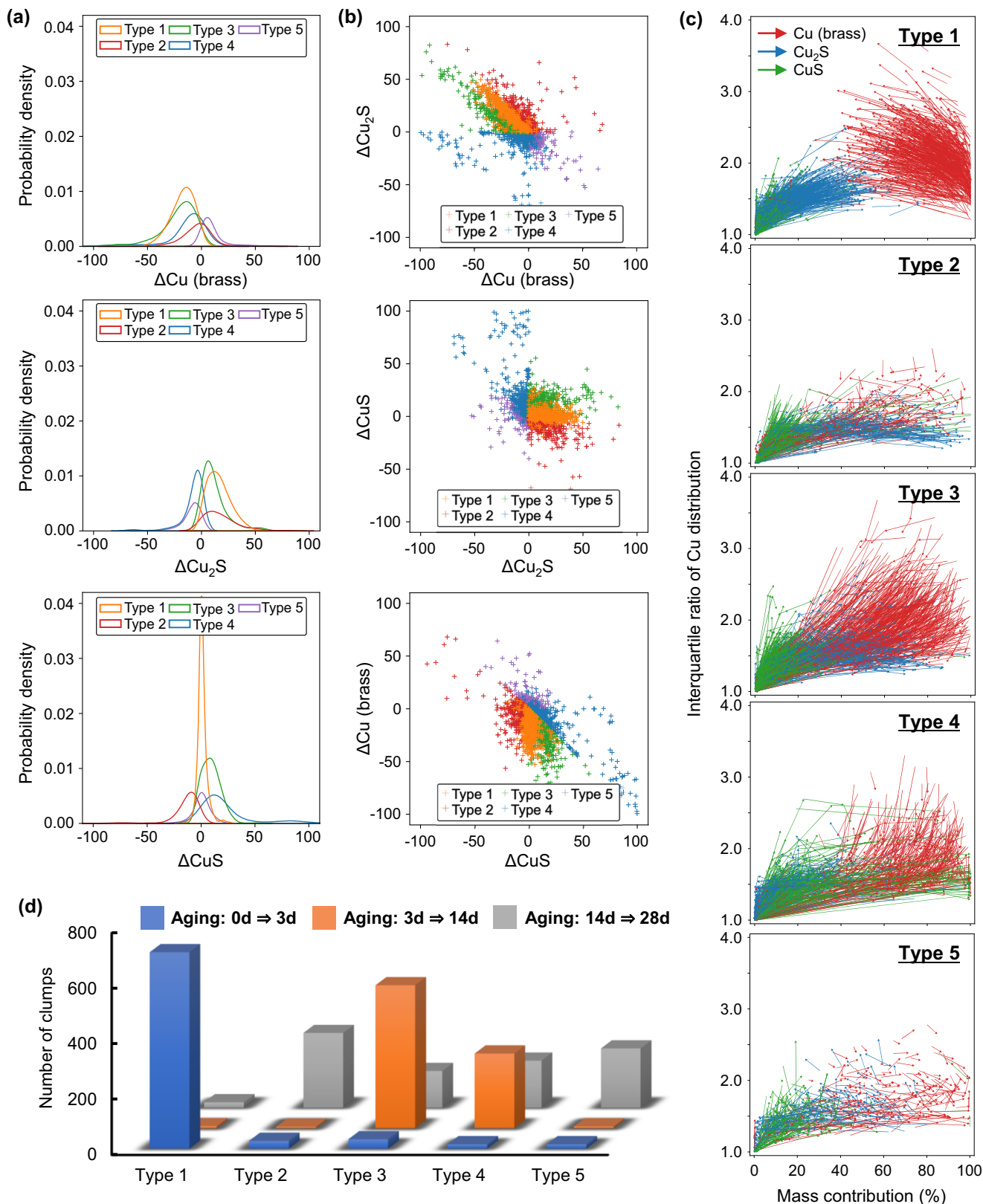


Fig. 4 Unsupervised learning analysis to group the type of Cu sulfurization reactions. **a** Classification of the Cu reactions in the rubber/brass composite into types 1-5, **(b)** 2D plots of changes in the amounts of the three Cu components in the five reaction types, and **(c)** reaction vectors of types 1-5 inferred by the unsupervised learning method using Gaussian mixture model. **d** Number of clumps classified as types 1-5 in the three aging steps.

Cu sulfides, and their spatial and temporal changes in the rubber composite allowed the statistical analysis of the reaction behaviors of the rubber/brass interface. Data-driven unsupervised machine-learning informatics revealed the five reaction types of Cu sulfidation in the rubber composite and the sharp transitions of the reaction types from the enhancement to the embrittlement of adhesive features in the aging process.

Methods

Sample and aging. A rubber sample containing brass powders was prepared by mixing a rubber source and brass powders (3L7, Daiya Kogyo Co., Ltd.; Cu_{0.75}Zn_{0.25}, φ3 μm × 0.2 μm; 1 wt % with respect to rubber) and molded into a cylinder of φ700 μm (Supplementary Methods 1). The molded sample was vulcanized at 443 K for 10 min (**Aging-0**). The sample was subjected to the first aging treatment of heating at 343 K and a relative humidity of 96% for 3 days (**Aging-3**). After XAFS-CT measurements of the sample, the second aging treatment was conducted for 11 days under the same conditions; thus, the total aging time was 14 (= 3 + 11) days (**Aging-14**). The final aging treatment was carried out under the same conditions for 14 days (**Aging-28**).

3D-XAFS-CT measurements. Cu *K*-edge XAFS-CT measurements were performed at the BL36XU beamline, SPring-8, Japan (8 GeV, 100 mA)⁴³. The rubber/brass composite sample was inserted into a polyimide tube of φ800 μm (PIT-S-09, Hagitech) and was mounted perpendicular to the X-ray optical path on a rotating sample stage. Rotation angle θ was defined as the angle between the direction of the X-ray optical path and the orientation of the sample on the stage, and the perpendicular irradiation of the sample surface with monochromatized X-rays was at $\theta = 0^\circ$ (Supplementary Methods 2). The sample was irradiated with hard X-rays monochromatized through Si(111) channel-cut crystals at angle θ from -90° to 90° in 1° steps (Supplementary Fig. 8), and the X-ray transmission images of the sample were recorded by a high-resolution X-ray imaging unit (AA50, Hamamatsu Photonics, K.K.) coupled with a low-noise sCMOS camera (Orca-Flash 4.0, Hamamatsu Photonics, K.K.). The effective view size was 1330 μm × 1330 μm with a pixel size of 0.65 μm × 0.65 μm. For each dataset, a quick scan of the transmission XANES ($E = 8857\text{--}9357$ eV; 1400 points, 28 s) was performed at every θ , and the total measurement time of the Cu *K*-edge XAFS-CT scan was 1.5 h for a sample.

Data processing of XAFS-CT data. Four-dimensional transmission images (2D images ($X'Z'$) with energy scan (E) and sample-rotation scan (θ)) were converted into the absorption coefficient (μt ($X'Z'-E-\theta$)) by Beer's law (Supplementary Methods 3). The μt data was spatially binned into 2 pixels × 2 pixels (1.30 μm × 1.30 μm) and smoothed the energy dimension to decrease the data points from 1400 pts to 384 pts. The series of XANES spectra was fitted by using Eq. 1 with the linear combination of the XANES spectra of three standard samples (Cu (brass), Cu₂S, and CuS).

$$\mu t = a_0 + a_1 \times (E - E_0) + b_1 \times I_{Cu(\text{brass})} + b_2 \times I_{Cu_2S} + b_3 \times I_{CuS} \quad (1)$$

The 3D matrices ($X'Z'-\theta$) of a_0 (sample morphology) and the coefficients of Cu (brass) (b_1), Cu₂S (b_2), and CuS (b_3) in the $X'Z'$ projection coordinates along θ were converted into the sinograms of $X'\theta$ cross-sections along Z' ($X'\theta-Z'$). The converted sinograms of the parameters were reconstructed into the 3D matrices (XYZ) of the parameters in real space by the ordered-subset expectation maximization method (Supplementary Methods 3). The threshold of the noise level of the reconstructed data was defined as

0.0002 (Supplementary Methods 3, Supplementary Fig. 9) and the reconstructed data are presented in Figs. 1, 2 considering the threshold level.

Data mining of the 3D images. The sets of reconstructed XAFS-CT data for the rubber/brass composite were preprocessed, and the auto-identification and matching of isolated Cu clumps in the sample at each aging time were conducted (Supplementary Methods 4). Hierarchical density-based spatial clustering of applications with noise analysis was performed on the extracted cylinder images to extract the shape and coordinate information of all the Cu clumps dispersed in the sample⁴⁸. The same process was performed on the XAFS-CT data at other aging times and the 3D coordinates of the samples at different aging times were corrected computationally. The outer 75% of the cylindrical region with the top 95 layers and the bottom 25 layers in the depth direction (along the *Z*-axis) were excluded, and the trimmed region was used for further informatics analysis.

The outer surface of the identified Cu clumps was defined using a threshold value of 0.0003. The surface was detected using a gradient-based edge detection algorithm⁴⁹, widely used in image processing to find object boundaries in images (Supplementary Methods 4). The distances from the voxels of each clump to the clump surface were then calculated. For each voxel in the 3D box, we searched for the nearest voxel belonging to the detected surface to measure the shortest path from the voxel to the detected surface. To resolve the nearest-neighbor search problem, we performed the search in the nearest-neighbor graph⁵⁰, constructed by the KD-tree algorithm.

For each clump, the mass contributions of the three Cu components and the interquartile ratio of the intensity distribution of voxels were used as descriptors for representing the valence state components of the clump. The log-normal distribution was used to fit the intensity data of each valence state component in the clumps and the interquartile ratio, which is defined as the ratio between the 25th and 75th percentiles of the data, was selected as the second descriptor. Unsupervised learning analysis with Gaussian mixture model algorithms was used for grouping the changes in the amounts of the three components (ΔCu (brass), $\Delta\text{Cu}_2\text{S}$, and ΔCuS) of the clumps during the three aging steps⁵¹. To group reactions with similar types of Cu changes, this probabilistic model assumed all the data instances were generated from a mixture of a finite number of Gaussian distributions with unknown parameters. All the 2406 extracted reactions were divided into five distinct groups with different types of Cu changes (Supplementary Methods 4).

Data availability

The data are available from the corresponding authors upon reasonable request.

Received: 30 March 2023; Accepted: 6 October 2023;
Published online: 06 November 2023

References

1. Crowther, B. G. (Ed.) *Handbook of rubber bonding*, (Rapra Technology Ltd, UK, 2001).
2. Van Ooij, W. J., Harakuni, P. B. & Buytaert, G. Adhesion of steel tire cord to rubber. *R. Chem. Technol.* **82**, 315–339 (2009).
3. Van Ooij, W. J. Mechanism and theories of rubber adhesion to steel tire cords—An overview. *R. Chem. Technol.* **57**, 421–456 (1984).
4. Van Ooij, W. J. Fundamental aspects of rubber adhesion to brass-plated steel tire cords. *R. Chem. Technol.* **52**, 605–675 (1979).
5. Ozawa, K. et al. Angle-resolved HAXPES investigation on the chemical origin of adhesion between natural rubber and brass. *Langmuir* **33**, 9582–9589 (2017).

6. Fulton, W. S., Sykes, D. E. & Smith, G. C. SIMS depth profiling of rubber-tyre cord bonding layers prepared using ^{64}Zn depleted ZnO. *Appl. Surf. Sci.* **252**, 7074–7077 (2006).
7. Kim, J. M. & Van Ooij, W. J. Study of Rubber-Brass Adhesion Mechanism by Secondary Ion Mass Spectrometry. *R. Chem. Technol.* **75**, 199–214 (2002).
8. Van Ooij, W. J. The role of XPS in the study and understanding of rubber-to-metal bonding. *Surf. Sci.* **68**, 1 (1977).
9. Kurbatov, G. G., Beshenkov, V. G. & Zaporozhenko, V. I. AES and factor analysis study of cord-oxidized brass layers and rubber-to-brass interface chemical composition. *Surf. Interfac. Anal.* **17**, 779–785 (1991).
10. Chandra, A. K., Mukhopadhyay, R., Konar, J., Ghosh, T. B. & Bhowmic, A. K. X-ray photoelectron spectroscopy and Auger electron spectroscopy of the influence of cations and anions of organometallic adhesion promoters on the interface between steel cord and rubber skim compounds. *J. Mat. Sci.* **31**, 2667–2676 (1996).
11. Buytaert, G., Coornaert, F. & Dekeyser, W. Characterization of the steel tire cord–rubber interface. *R. Chem. Technol.* **82**, 430–441 (2009).
12. Ashirgade, A., Harukuni, P. B., Van & Ooij, W. J. Effects of Aging on the Morphology of Rubber-Brass Interfacial Layer. *Tire Sci. Technol.* **39**, 20–43 (2011).
13. Patil, P. Y. & Van Ooij, W. J. Mechanistic study of the effect of adhesion-promoter resins on the crystal structure of the copper sulfide adhesion layer at the rubber-brass interface. *R. Chem. Technol.* **79**, 82–93 (2006).
14. Ishikawa, Y. Effects of compound formulation on the adhesion of rubber to brass-plated steel cord. *R. Chem. Technol.* **57**, 855–878 (1984).
15. Kannan, M. P. et al. Nonstoichiometric copper sulfide nanostructures at the brass-rubber interface: Implications for rubber vulcanization temperature in the tire industry. *ACS Appl. Nano Mater* **3**, 7685–7694 (2020).
16. Ozawa, K. & Mase, K. Evidence for chemical bond formation at rubber–brass interface: Photoelectron spectroscopy study of bonding interaction between copper sulfide and model molecules of natural rubber. *Surf. Sci.* **654**, 14–19 (2016).
17. Ozawa, K. et al. High-resolution photoelectron spectroscopy study of degradation of rubber-to-brass adhesion by thermal aging. *Appl. Surf. Sci.* **268**, 117–123 (2013).
18. Ozawa, K. et al. High-resolution photoelectron spectroscopy analysis of sulfidation of brass at the rubber/brass interface. *Appl. Surf. Sci.* **264**, 297–304 (2013).
19. Hotaka, T., Ishikawa, Y. & Mori, K. Characterization of Adhesion Interlayer Between Rubber and Brass by a Novel Method of Sample Preparation. *R. Chem. Technol.* **80**, 61–82 (2007).
20. Fulton, W. S., Smith, G. C. & Titchener, K. J. Interfacial microanalysis of rubber-tyre-cord adhesion and the influence of cobalt. *Appl. Surf. Sci.* **221**, 69–86 (2004).
21. Ozawa, K. et al. In situ chemical state analysis of buried polymer/metal adhesive interface by hard X-ray photoelectron spectroscopy. *Appl. Surf. Sci.* **320**, 177–182 (2014).
22. Kakubo, T. et al. Degradation of a Metal-Polymer Interface Observed by Element-Specific Focused Ion Beam-Scanning Electron Microscopy. *Langmuir* **36**, 2816 (2020).
23. Shimizu, K., Miyata, T., Nagao, T., Kumagai, A. & Jinnai, H. Visualization of the tensile fracture behaviors at adhesive interfaces between brass and sulfur-containing rubber studied by transmission electron microscopy. *Polymer* **181**, 121789 (2019).
24. Yamauchi, M. T. et al. Examination of rubber adhesion property of brass film on steel formed by magnetron sputtering. *R. Chem. Technol.* **78**, 105–113 (2005).
25. Chen, Y. & Schlarb, J. L. Steel Cord–Rubber Adhesion with SEM/EDX. *Tire Sci. Technol.* **46**, 27–37 (2018).
26. Holtkamp, D., Elschner, A., Müller, G. & Pieroth, M. Novel model system to study the influence of rubber compound formulation on the structure and composition of the rubber brass interphase. *Surf. Interfac. Anal.* **23**, 155–162 (1995).
27. Jeon, G. S., Han, M. H. & Seo, G. Enhancing adhesion properties between rubber compound and brass-plated steel cord by incorporating silica into rubber. *J. Adhes. Sci. Technol.* **13**, 153–168 (1999).
28. Patil, P. Y. & Van Ooij, W. J. Mechanism of Improved Aged Rubber-to-Brass Adhesion Using One-Component Resins. *R. Chem. Technol.* **78**, 155–173 (2005).
29. Shinohara, Y. et al. Microscopic structural response of nanoparticles in styrene-butadiene rubber under cyclic uniaxial elongation. *Polym. J.* **51**, 161–171 (2019).
30. Shinohara, Y., Seike, H., Kishimoto, H., Tamenori, Y. & Amemiya, Y. Distribution of sulfur in styrene-butadiene rubber studied with anomalous small-angle X-ray scattering at sulfur K-edge. *Polymer* **105**, 368–377 (2016).
31. Mashita, R., Yashiro, W., Kaneko, D., Bito, Y. & Kishimoto, H. High-speed rotating device for X-ray tomography with 10 ms temporal resolution. *J. Synchrotron Rad.* **29**, 322–326 (2021).
32. Euchler, E. et al. First-time investigations on cavitation in rubber parts subjected to constrained tension using in situ synchrotron X-ray microtomography (SR μ CT). *Adv. Eng. Mater.* **23**, 2001347 (2021).
33. Federico, C. E., Rauchs, G., Kotecky, O., Westermann, S. & Addiego, F. Cavitation in thermoplastic-reinforced rubber composites upon cyclic testing: Multiscale characterization and modelling. *Polymer* **211**, 123084 (2020).
34. Kishimoto, H. et al. Visualization of nanoscale deformation in polymer composites with zernike-type phase-contrast X-ray microscopy and the finite element method. *Polym. J.* **45**, 64–69 (2013).
35. Becher, J. et al. Chemical gradients in automotive Cu-SSZ-13 catalysts for NO_x removal revealed by operando X-ray spectromicroscopy. *Nat. Catal.* **4**, 46–53 (2021).
36. Sanchez, D. F. et al. Spatio-chemical heterogeneity of defect-engineered metal–organic framework crystals revealed by full-field tomographic X-ray absorption spectroscopy. *Angew. Chem. Int. Ed.* **60**, 10032–10039 (2021).
37. Schmidt, J. E., Oord, R., Guo, W., Poplawsky, J. D. & Weckhuysen, B. M. Nanoscale tomography reveals the deactivation of automotive copper-exchanged zeolite catalysts. *Nat. Commun.* **8**, 1666 (2017).
38. Zhang, J. et al. Depth-dependent valence stratification driven by oxygen redox in lithium-rich layered oxide. *Nat. Commun.* **11**, 6342 (2020).
39. Matsui, H. et al. Operando 3D visualization of migration and degradation of Pt cathode catalyst in a polymer electrolyte fuel cell. *Angew. Chem. Int. Ed.* **56**, 9371–9375 (2017).
40. Matsui, H. et al. Variation of local structure and reactivity of Pt/C catalyst for accelerated degradation test of polymer electrolyte fuel cell visualized by operando 3D CT-XAFS imaging. *ChemNanoMat* **8**, e202200008 (2022).
41. Tan, Y. et al. PtCo/C cathode catalyst degradation in a polymer electrolyte fuel cell investigated by an infographic approach combining three-dimensional spectroimaging and unsupervised learning. *J. Phys. Chem. C* **123**, 18844–18853 (2019).
42. Matsui, H. et al. Operando XAFS Imaging of Distribution of Pt Cathode Catalysts in PEFC MEA. *Chem. Rec.* **19**, 1380–1392 (2019).
43. Uruga, T. et al. Spring-8 BL36XU: Synchrotron radiation X-ray-based multi-analytical beamline for polymer electrolyte fuel cells under operating conditions. *Chem. Rec.* **19**, 1444–1456 (2019).
44. Ikeda, Y. et al. Roles of Dinuclear Bridging Bidentate Zinc/Stearate Complexes in Sulfur Cross-Linking of Isoprene Rubber. *Organometallics* **38**, 2363–2380 (2019).
45. Li, J. et al. Dynamics of particle network in composite battery cathodes. *Science* **376**, 517 (2022).
46. Jiang, Z. et al. Machine-learning-revealed statistics of the particle-carbon/binder detachment in lithium-ion battery cathodes. *Nat. Commun.* **11**, 2310 (2020).
47. Hirose, M. et al. Oxygen-diffusion-driven oxidation behavior and tracking areas visualized by X-ray spectro-ptychography with unsupervised learning. *Commun. Chem.* **2**, 50 (2019).
48. Campello, R. J. G. B., Moulavi, D. & Sander, J. Density-Based Clustering Based on Hierarchical Density Estimates. *PAKDD 2013, Part II, LNAI 7819*, 160 (2013).
49. Shrivakshan, G. T. & Chandrasekar, C. A. Comparison of various edge detection techniques used in image processing. *Int. J. Comput. Sci. Issues* **9**, 269 (2012).
50. Lee, D. T. & Wong, C. K. Worst-case analysis for region and partial region searches in multidimensional binary search trees and balanced quad trees. *Acta Inform.* **9**, 23 (1977).
51. Xu, L. & Jordan, M. I. On convergence properties of the EM algorithm for gaussian mixtures. *Neural. Comput.* **8**, 129–151 (1996).

Acknowledgements

This work was supported by JST CREST Grant Number JPMJCR2235 (Innovative Measurement and Analysis), collaborative research with The Yokohama Rubber Co. Ltd., a JSPS KAKENHI Grant-in-Aid for Scientific Research (B) (22H02031), (C) (20K05301), and (JP19H05815), and the R-ing (Reaction Infography) World Research Unit (B-1) at Nagoya University. XAFS-CT measurements were supported by RIKEN Spring-8 Center, Japan.

Author contributions

H. M. carried out XAFS-CT measurements and the developments of XAFS-CT analysis. Y. M. carried out the measurement and analysis of XAFS-CT. R. N. analyzed XAFS data. T. K. and N. A. prepared samples and performed the degradation treatments of the samples. T. U. contributed to the development and setup of the XAFS-CT measurements. M. H., D. D., and H. D. carried out the informatics analysis of the XAFS-CT data. M. T. conceived the project, directed this study, and wrote the paper.

Competing interests

The authors declare no competing interests.

Additional information

Supplementary information The online version contains supplementary material available at <https://doi.org/10.1038/s43246-023-00413-z>.

Correspondence and requests for materials should be addressed to Hieu-Chi Dam or Mizuki Tada.

Peer review information *Communications Materials* thanks Ken Kojio, Graham Smith and the other, anonymous, reviewer(s) for their contribution to the peer review of this work. Primary Handling Editor: Jet-Sing Lee. A peer review file is available.

Reprints and permission information is available at <http://www.nature.com/reprints>

Publisher's note Springer Nature remains neutral with regard to jurisdictional claims in published maps and institutional affiliations.



Open Access This article is licensed under a Creative Commons Attribution 4.0 International License, which permits use, sharing, adaptation, distribution and reproduction in any medium or format, as long as you give appropriate credit to the original author(s) and the source, provide a link to the Creative Commons licence, and indicate if changes were made. The images or other third party material in this article are included in the article's Creative Commons licence, unless indicated otherwise in a credit line to the material. If material is not included in the article's Creative Commons licence and your intended use is not permitted by statutory regulation or exceeds the permitted use, you will need to obtain permission directly from the copyright holder. To view a copy of this licence, visit <http://creativecommons.org/licenses/by/4.0/>.

© The Author(s) 2023